# Optical properties of $Ti_xSi_{1-x}O_2$ solid solutions

Pavel Ondračka,[1,2,*] David Holec,[3] David Nečas,[2] Eva Kedroňová,[1,2] Stéphane Elisabeth,[4] Antoine Goullet,[4] and Lenka Zajíčková[1,2]

[1]*Department of Physical Electronics, Faculty of Science, Masaryk University, Kotlářská 2, 611 37 Brno, Czech Republic*

[2]*CEITEC - Central European Institute of Technology, Masaryk University, Purkyňova 123, 612 00 Brno, Czech Republic*

[3]*Department of Physical Metallurgy and Materials Testing, Montanuniversität Leoben, Franz-Josef-Straße 18, A-8700 Leoben, Austria*

[4]*Institut des Matériaux Jean Rouxel (IMN), Université de Nantes, UMR CNRS 6502, 2 rue de la Houssinière, BP 32229, 44322 Nantes Cedex 3, France*

(Received 9 January 2017; revised manuscript received 20 April 2017; published 30 May 2017)

In this work, we use density functional theory to predict the optical properties of $Ti_xSi_{1-x}O_2$ solid solutions. The special quasirandom structure method and the simulated annealing procedure were applied to produce models of crystalline and amorphous $Ti_xSi_{1-x}O_2$. These were fully structurally optimized by using the VASP package, while their electronic structure and optical properties were subsequently calculated by using the WIEN2k package employing the TB-mBJ potential. The calculated band gaps for a-$Ti_xSi_{1-x}O_2$ evaluated by using the Tauc-like fitting approach are 8.53 eV for $SiO_2$, quickly decreasing to 4.0 eV at $x = 0.19$, 3.52 eV at $x = 0.34$, and 3.24 eV for $TiO_2$. Experimental samples were prepared by means of plasma-enhanced chemical vapor deposition to support the calculations. Ellipsometry and spectrophotometry yield a compositional trend for the experimental optical band gap comparable with our predictions: a quick decrease from 7.94 eV for pure $SiO_2$ to 3.91 eV at $x = 0.15$, followed by a much slower decrease over the rest of the composition range ending at 3.26 eV for pure $TiO_2$. A detailed analysis of anatase and rutile-based solid solutions reveals the introduction of silicon-induced oxygen states into the band gap in the $TiO_2$-rich composition region, which results in the predicted reduction of the band gap. However, we show that the optical absorption of those states is negligible. We have obtained good agreement between the calculated and measured imaginary part of the dielectric function $\varepsilon_i$, especially for the $TiO_2$-rich compositions. Finally, we predict an almost-linear refractive index change at 632.8 nm between a-$SiO_2$ (1.36) and a-$TiO_2$ (2.34), which was experimentally confirmed.

DOI: 10.1103/PhysRevB.95.195163

## I. INTRODUCTION

Fine tuning of optical properties of thin films is of great importance for applications such as antireflective coatings [1], laser mirrors [2], or rugate filters [3]. It has been shown that mixing $TiO_2$ with $SiO_2$ can be used to control its optical properties [4,5]. Due to the big differences in $TiO_2$ and $SiO_2$ refractive indices (∼2.45 and ∼1.45 [6]) and optical band gaps (∼8.9 eV [7] and ∼3.2 eV [8]) there is huge space for composition-induced tuning of optical properties. Moreover, it can also help to overcome some shortcomings of pure $TiO_2$ films, such as the columnar morphology [4], which leads to increased optical losses and degradation of its insulating behavior. Mixing SiO and TiO bonds leads to more homogeneous and amorphous material with a columnar character being less pronounced in comparison with pure $TiO_2$ films [4,6].

$TiO_2$–$SiO_2$ films deposited by various techniques, such as plasma-enhanced chemical vapor deposition (PECVD) [4,9], ion-beam sputtering [5], electron-beam coevaporation [6], the sol-gel method [10], or plasma sputtering [11], have attracted much experimental efforts. However, while numerous theoretical calculations of structural [12], elastic [13,14], electronic, and optical [15–18] properties of pure $TiO_2$ and $SiO_2$ were published, far less attention has been paid to theoretical calculations of properties of $Ti_xSi_{1-x}O_2$. Besides, the published theoretical work is focused mainly on the atomic structure of $Ti_xSi_{1-x}O_2$ [19,20], while an in-depth study of $Ti_xSi_{1-x}O_2$ electronic structure and optical properties is still missing.

To predict the optical properties from first principles by using the density functional theory (DFT), it is necessary to ensure that the electronic structure and band-gap value are calculated accurately. The band gap is known to be underestimated by conventional approximations for the exchange-correlation (xc) potential, local density approximation (LDA), and generalized gradient approximation (GGA). Recently, Tran and Blaha [21] proposed a new semilocal xc potential (Tran–Blaha modified Becke–Johnson, TB-mBJ) which yields highly accurate energy band gaps in most semiconductors and insulators [22]. The clear improvement towards experimental values using the TB-mBJ potential instead of the conventional GGA was demonstrated by Sai and Bang-Gui [16]. In the case of $TiO_2$, the band-gap values predicted by GGA are 1.89 and 2.12 eV for rutile and anatase, respectively, while the TB-mBJ potential gives values of 2.60 and 3.01 eV. A further optimization of the mBJ parameters has led to even better agreement than the original parametrization [23]. Sai and Bang-Gui showed the huge impact of the improved description of the electronic structure on the predicted optical properties, such as refractive index, $n$, extinction coefficient, $\kappa$, or dielectric function $\varepsilon$, when employing the TB-mBJ potential for the case of rutile and anatase $TiO_2$ [16].

In this work, we predict the compositionally dependent structural, electronic, and optical properties of $Ti_xSi_{1-x}O_2$ and compare them with experimental optical constants measured over a broad spectral range from the near infrared (NIR) up to

*pavel.ondracka@gmail.com

 

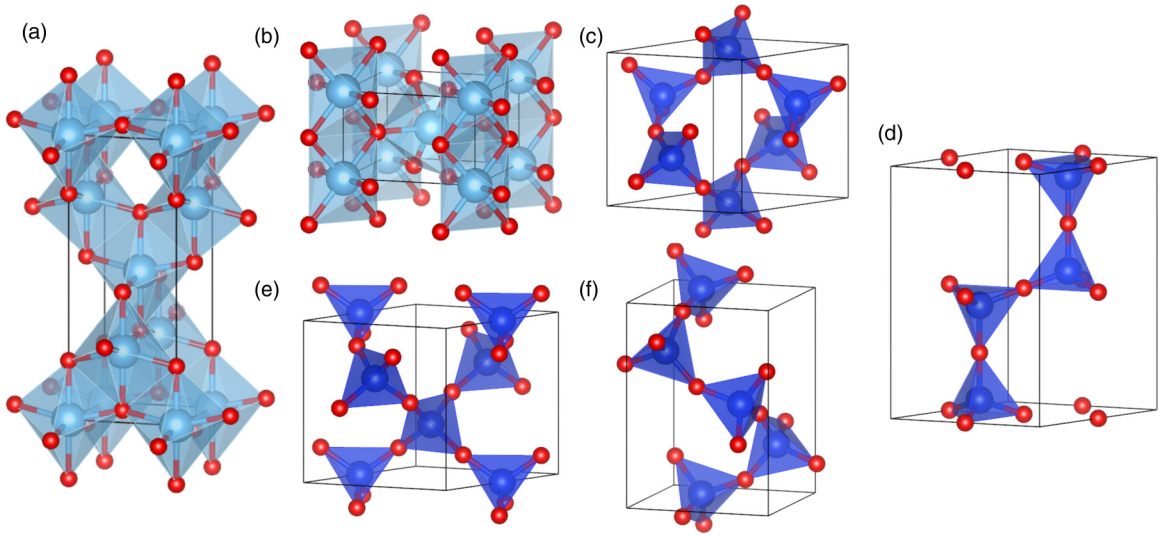


FIG. 1. Crystal structure of all calculated crystalline polymorphs with highlighted polyhedra: (a) anatase, (b) rutile, (c) $\alpha$-quartz, (d) $\beta$-tridymite, (e) $\beta$-quartz, (f) $\alpha$-cristobalite. Visualized by VESTA [24].

the vacuum ultraviolet (VUV) range on $Ti_xSi_{1-x}O_2$ samples prepared by means of PECVD.

## II. METHODOLOGY

### A. Calculations

Two classes of disordered structures were studied: crystalline solid solutions and amorphous materials. A special quasirandom structure (SQS) method [25] was used to generate structural models of $Ti_xSi_{1-x}O_2$ crystalline solid solutions based on the anatase and rutile $TiO_2$ phases, and $\alpha$-quartz, $\beta$-quartz, $\alpha$-cristobalite, and $\beta$-tridymite $SiO_2$ phases (Fig. 1) as the most common $TiO_2$ and $SiO_2$ crystalline structures. There is some overlap between the $SiO_2$ and $TiO_2$ structures, e.g., the $SiO_2$ high-pressure stishovite polymorph has the rutile structure, and it has been shown that $TiO_2$ can be stabilized in the tridymite structure [26]. The supercell sizes were chosen to be as cubic as possible (hence to guarantee equivalent separation distances between any atom and its periodic images in all directions) and to contain around 50–100 atoms. This yielded a $3 \times 3 \times 1$ supercell with 108 atoms for anatase, $2 \times 2 \times 4$ with 96 atoms for rutile, $2 \times 2 \times 2$ with 72 atoms for $\alpha$-quartz, $2 \times 2 \times 2$ with 72 atoms for $\beta$-quartz, $2 \times 2 \times 1$ with 48 atoms for $\alpha$-cristobalite, and $2 \times 2 \times 1$ with 48 atoms for $\beta$-tridymite. The supercells were structurally optimized (i.e., optimized with respect to the cell shape, volume, and atomic positions).

Simulation cells for the amorphous $Ti_xSi_{1-x}O_2$ were prepared by a simulated annealing procedure [27] using a similar protocol as in our previous study on $HfO_2$ [28]. Seven amorphous cells, each containing 96 atoms (64 oxygen and 32 Ti or Si atoms), and corresponding to $x = 0$ (32 Si), $x = 0.1875$ (26 Si + 6 Ti), $x = 0.34375$ (21 Si + 11 Ti), $x = 0.5$ (16 Si + 16 Ti), $x = 0.65625$ (11 Si + 21 Ti), $x = 0.8125$ (6 Si + 26 Ti), and $x = 1$ (32 Ti) were prepared. We note that "inverse" compositions, i.e., $x$ and $1 - x$, were generated independently. At the beginning, the 96 atoms were randomly distributed inside each cell—a cubic simulation box with a fixed side, given by the mass density of a given composition $x$. The densities were linearly interpolated between 3.8 and 2.2 g/cm$^3$, the common values for amorphous $TiO_2$ and $SiO_2$ [29,30]. Atoms inside the cells were thermally equilibrated by using an *ab initio* molecular dynamics run at 5000 K for 3 ps (time step of 3 fs). In the next step, the cell temperature was decreased to 0 K in 1000 steps, each corresponding to 3 fs. Finally, the resulting models were structurally relaxed with respect to atomic positions (at fixed volume).

The DFT calculations were performed using the Vienna Ab initio Simulation Package (VASP) [31,32] working with projector augmented method-capable pseudopotentials [33] describing electron-ion interactions. The quantum mechanical electron-electron exchange and correlation effects were included within the framework of generalized gradient approximation as parametrized by Perdew, Burke and Ernzerhof (GGA-PBE) [34]. Plane wave cut-off energy of 500 eV for crystalline and 400 eV for amorphous structures were used together with Monkhorst–Pack $k$-point meshes [35] with densities at least 120 $k$-point/Å$^{-3}$.

The electronic structure and optical properties were predicted by using the linearized augmented plane-wave method as implemented in the WIEN2k full potential all electron code [36] together with the modified Becke–Johnson potential allowing for a precise prediction of the band gap [21]. Optimized values of TB-mBJ parameters according to Koller *et al.* [23] ($A = 0.488$, $B = 0.5$, $e = 1$) were employed. Dense Monkhorst–Pack $k$-point meshes with densities at least 1400 $k$-point/Å$^{-3}$ were used for the calculation of optical properties. The $R_{\mathrm{mt}}K_{\mathrm{max}}$ matrix size parameter was set to 7.0 and the atomic sphere radii were set to almost touching spheres corresponding to roughly 1.7, 1.5, and 1.5 Bohr radii for Ti, Si, and O atoms, respectively. Optical properties were calculated by the optic code [37], a part of the WIEN2k package. It uses the random-phase approximation (RPA) to calculate the optical properties without the local field effects. Gaussian broadening of 0.1 eV was applied to the dielectric function in

order to better match room-temperature experimental optical measurements.

### B. Film deposition and characterization

The experimental samples in the form of thin films were deposited in a low-pressure high-density plasma reactor described in detail elsewhere [38]. The apparatus consists of an inductively coupled plasma (ICP) source and a diffusion chamber mounted below the source. The ICP was ignited by applying the radio frequency voltage (13.56 MHz) to an external helicon antenna. The PECVD of $Ti_xSi_{1-x}O_2$ worked in the mixture of oxygen, hexamethyldisiloxane vapor ($C_6H_{18}OSi_2$, HMDSO, 98%, Sigma Aldrich Ltd.) was used as the silicon precursor, and titanium isopropoxide vapor ($Ti(–OC_3H_7)_4$, titanium isopropoxide, 99.999%, Sigma Aldrich Ltd.) was used as the titanium precursor. Oxygen was introduced at the top of the ICP source, while both precursors were injected into the diffusion chamber via a dispersal ring, 15 cm in diameter, located 8 cm above the substrate. The titanium isopropoxide (TTIP) vapor was kept in a heated container (60 °C) and introduced through a heated line (63 °C) with a MKS mass flow meter (80 °C). Another MKS mass flow meter was used to control the amount of HMDSO vapor. HMDSO was kept in a container heated to 35 °C and the vapor was injected into the diffusion chamber through a line heated to 40 °C. Both precursors were introduced into the chamber at the same time. The film composition was varied by changing the flow rate of HMDSO (from 0 to 0.083 sccm) while keeping the flow rate of TTIP and $O_2$ constant. The deposition times were carefully selected to keep the film thickness around 250 nm. Crystalline (1 0 0)-orientated silicon wafers with thickness of $(381 \pm 25)\ \mu$m were used as substrates for the deposited films. The substrate holder was at the floating potential.

Chemical composition of the samples was determined by x-ray photoelectron spectroscopy (XPS) using a Kratos Axis Ultraspectrometer with Al $K_\alpha$ radiation at 1486.6 eV with the CasaXPS software.

X-ray diffraction analysis was performed by using a 3 kW Smartlab device from Rigaku using the Cu $K_\alpha$ source. The diffractometer was set up in a grazing-incidence geometry by using a parallel beam and a linear Dtex Ultradetector.

The samples were optically characterized by using a Jobin–Yvon VUV ellipsometer in a spectral range 0.56–8.7 eV at an angle of incidence of 70° and the vacuum ultraviolet spectrometer McPherson VUVAS 1000 in a spectral range 5.6–10.3 eV at near-normal angle of incidence. The optical data of all samples were fit by using a structural model including a surface roughness described by the Rayleigh–Rice theory [39,40], a $Ti_xSi_{1-x}O_2$ layer described by the so-called universal dispersion model based on the parametrization of the joint density of states for valence-to-conduction interband transitions [41–43], and a Si substrate modelled by a sum-rule-based dispersion model of crystalline silicon [44]. For Ti-rich samples a model of vertical inhomogeneity of the $Ti_xSi_{1-x}O_2$ layer was needed in order to obtain a good fit of the experimental data. The optical constants of the films were modelled as a linear transition between optical constants at the top $\hat{\varepsilon}_{\text{top}}$ and bottom $\hat{\varepsilon}_{\text{bot}}$ of the layer. The $\hat{\varepsilon}_{\text{top}}$ was governed by the dispersion model, while the optical constants at the bottom were calculated as $\hat{\varepsilon}_{\text{bot}} = 1 + f_{\text{inhom}}(\hat{\varepsilon}_{\text{top}} - 1)$, where $f_{\text{inhom}}$ is the fitted inhomogeneity factor. Additionally, a 2-nm-thick $SiO_2$ layer was considered between the Si substrate and the $Ti_xSi_{1-x}O_2$ layer and on the backside of the sample by using the $SiO_2$ table values [45], because the native oxide was not cleaned before the deposition. The newAD2 software was used for analysis of the optical data [46].

## III. RESULTS AND DISCUSSION

### A. Film structure and composition

XRD results revealed a crystalline character of the pure $TiO_2$ sample ($x = 1.0$); peak positions in the XRD pattern obtained correspond to the anatase structure with no preferred grain orientation. The other samples, i.e., those containing silicon, exhibited XRD-amorphous structure. This corresponds well with results on surface roughness, as determined from fitting of the optical measurements. All of the mixed films have quite smooth surface with roughness root mean square (rms) below 3 nm and only the $TiO_2$ film shows higher roughness rms of 12 nm. The XPS results showed that our films are not perfectly stoichiometric and have slight oxygen excess, e.g., with $y \approx 2.1$ in $Ti_xSi_{1-x}O_y$ as well as some carbon content. Rutherford backscattering spectrometry (RBS) and infrared spectroscopy measurements were done for a few selected samples to clarify this. RBS did not reveal a significant amount of carbon, hence the carbon content measured by XPS can be attributed to surface contamination. IR spectroscopy revealed the presence of the OH groups as a possible cause of the oxygen excess. However, none of those defects affects the measured optical properties significantly.

### B. Phase stability predictions

The most preferable phase at fixed composition, 0 K and no external pressure 0 Pa, is conveniently identified by the lowest energy of formation, $E_f$, among the considered polymorphs. $E_f$ is defined as

$$E_f(Ti_xSi_{1-x}O_2) = E_{\text{tot}}(Ti_xSi_{1-x}O_2) - \tfrac{1}{3}[xE_{\text{tot}}(Ti) + (1-x)E_{\text{tot}}(Si) + 2E_{\text{tot}}(O_2)], \quad (1)$$

where $E_{\text{tot}}(X)$ is the (*ab initio* calculated) total energy of $X$ (per atom); for the single component $X$, $E_{\text{tot}}(X)$ corresponds to hcp Ti, diamond Si, or molecular $O_2$.

Based on the energy of formation shown in Fig. 2, the anatase structure is expected to be stable from $x \approx 0.85$ to 1.0, while for lower Ti content the cristobalite structure is the most stable. This prediction at the Ti-rich end is in an apparent contradiction with the phase diagram [47], according to which the rutile phase is the stable one at 0 K. This is, however, a known deficiency of the standard LDA, GGA, or even the HSE06 potentials failing to correctly predict the ground state of $TiO_2$. Earlier reports showed that this issue can be resolved by employing the GGA + $U$ [48,49] or even GGA + $U$ together with van der Waals dispersive interactions [26]. Nevertheless, the exact value of the Hubbard on-site potential $U$ is material dependent and should be optimized against experiments, hence losing (partly) the predictive power of *ab initio* calculations. Interestingly, when using the TB-mBJ energies, the rutile $TiO_2$ becomes energetically preferable to

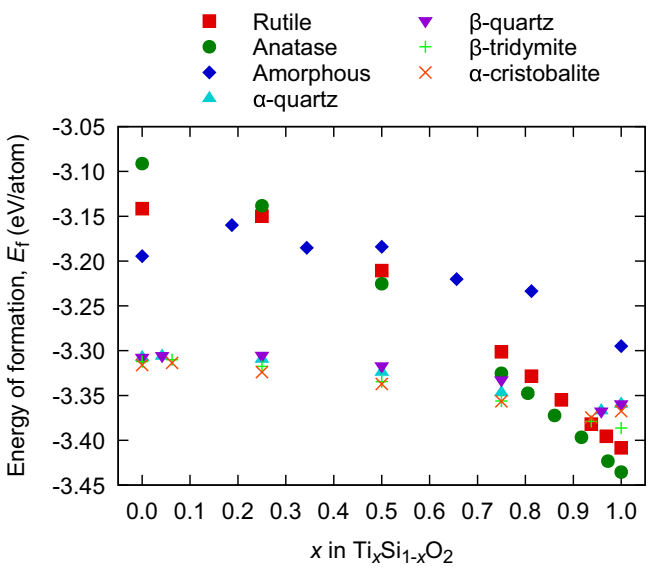


FIG. 2. Energy of formation, $E_f$, as a function of composition $x$ in the $TiO_2$–$SiO_2$ quasibinary system. In total seven polymorphs were considered.

the anatase structure. We note, however, that the TB-mBJ total energies are hard to interpret because there is no energy functional related to the TB-mBJ potential [21]. Regarding the Si-rich end, it is interesting to note that all four $SiO_2$-based polymorphs are energetically very close to each other, and in particular that the energies of $\alpha$-cristobalite and $\beta$-tridymite are almost overlapping. Similar results were reported earlier employing both LDA and GGA xc potentials [50] and were confirmed by employing evolutionary crystal structure prediction techniques by Oganov and Glass [51]. Moreover, these lowest-energy phases differ only in the arrangement of $XO_4$ ($X$ = Ti, Si) tetrahedrons, i.e., the building units forming the $SiO_2$-based structures. Consequently, a phase competition is expected which may be one of the reasons for the fact that $SiO_2$ is often synthesized with an amorphous structure. The models for amorphous structures yield energies of formation 0.1–0.15 eV/at. higher then the most preferable polymorph. This is not surprising since the entropic term, $-TS$, which compensates for the energy penalty of broken bonds, has no contribution at 0 K. Nonetheless, the amorphous phase is relevant for the interpretation of finite-temperature experiments [19] since, e.g., the energy difference between the crystalline phase with lowest energy and the amorphous structure was predicted to be almost twice as large for $HfO_2$ in which the amorphous phase is experimentally also obtained for thin films. Finally we note that all $E_f$ curves are concave, suggesting that a (small) driving force for isostructural decomposition into the boundary binary phases exists.

The major difference between $TiO_2$-based and $SiO_2$-based structures is the coordination number of the metal atom which is six in the former case and four in the latter case. We note that, consequently, the O atom coordination numbers are also different: three in $TiO_2$ and two in $SiO_2$ structures. Analysis of the average coordination numbers in the relaxed amorphous cells is shown in Fig. 3. The coordination numbers were obtained as number of atoms closer then fixed radius $r_{\min}$

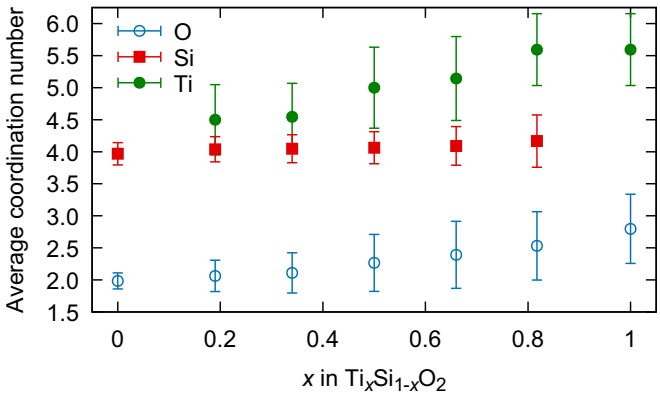


FIG. 3. Average coordination number for atoms in the amorphous structures, with spreads displayed using error bars corresponding to one standard deviation.

which was selected by using the value of the first minimum in the pair distribution function. The selected $r_{\min}$ values were 2.4 Å for Ti–Ti and Ti–Si pairs and 2.2 Å for the O–O pair. By using these cutoff distances, we found only Ti–O and Si–O bonds, in agreement with the expected cross-linking. It follows that while the average coordination numbers of Ti and O smoothly change from close to six and three on the Ti-rich side towards four and two on the Si-rich side, the coordination of Si atoms remains almost constant at four. This illustrates that Si is extremely "unhappy" in the six-coordinated environment, and hence its solubility in $TiO_2$-based structures is very limited, while the opposite holds for Ti in $SiO_2$-based structures (cf. Fig. 2). We note that, even though our coordination numbers are slightly lower than those reported by Landmann [19], which is due to the lower mass density assumed for the amorphous phase, they exhibit the same trends.

### C. Band structure and band gap

Our TB-mBJ electronic structure calculations predict an indirect electronic band gap of 3.09 eV for anatase and a direct electronic band gap of 2.62 eV for rutile, if calculated simply as the energy difference between highest occupied and lowest unoccupied state, i.e., highest occupied molecular orbital–lowest unoccupied molecular orbital (HOMO–LUMO) gap. These values are slightly higher than values by Sai and Bang-Gui [16] using the original TB-mBJ parametrization, and significantly larger than the standard GGA and LDA predictions.

For the $SiO_2$ crystal structures, we obtain an indirect band gap of 9.38 eV for $\alpha$-quartz, an indirect band gap of 9.19 eV for $\beta$-quartz, a direct gap of 9.72 eV for $\alpha$-cristobalite, and an indirect gap of 10.13 eV for $\beta$-tridymite. This is summarized in Table I along with the PBE values as well as reported values using the more advanced GW method based on many-body perturbation theory. While the band-gap values obtained with the TB-mBJ are a clear improvement over the PBE values, they are still underestimated with respect to the GW gaps. The absolute band-gap difference $E_g^{GW} - E_g^{TBmBJ}$ is similar for $TiO_2$ and $SiO_2$ (rutile: 0.84 eV, anatase: 0.64 eV, $\alpha$-quartz: 0.75 eV) so despite this slight underestimation a correct band-gap trend for the $Ti_xSi_{1-x}O_2$ can be expected.

TABLE I. Calculated electronic band gaps in eV for $SiO_2$ and $TiO_2$ crystals with PBE, TB-mBJ, and compared with the reported GW method results.

| | PBE | TB-mBJ | GW |
|---|---|---|---|
| Rutile | 1.82 | 2.62 ($\Gamma \rightarrow \Gamma$) | 3.46 [59] |
| Anatase | 2.09 | 3.09 ($0.82\Sigma \rightarrow \Gamma$) | 3.73 [59] |
| $\alpha$-quartz | 5.42 | 9.35 ($K \rightarrow \Gamma$) | 10.1 [18] |
| $\beta$-quartz | 5.54 | 9.19 ($0.72\Delta \rightarrow \Gamma$) | |
| $\beta$-tridymite | 5.37 | 10.13 ($0.95\Sigma \rightarrow \Gamma$) | |
| $\alpha$-cristobalite | 5.52 | 9.72 ($\Gamma \rightarrow \Gamma$) | |

It is worth noting that the majority of the literature reports the band gap of around 3 eV for rutile and 3.2 eV for anatase [8,52–54] and those are also the values that most *ab initio* predictions are compared with (for example [16,30,55,56]). However, these experimental band gaps originate from optical measurements and hence should not be directly compared with band gaps obtained just from the band-structure calculations (neglecting excitonic effects). In this regard the higher reported rutile band gaps of 3.3 eV by photoemission and bremsstrahlung isochromat spectroscopy [57] and 3.6 eV by ultraviolet photoemission and inverse photoemission spectroscopy [58] are better suited for comparison with band-structure calculations. Our predicted band gaps for $TiO_2$ are around 0.7 eV smaller than those experimental band gaps.

The evolution of the electronic band gap is shown in Fig. 4 for all calculated polymorphs. Both the experimental and calculated gaps show a nonlinear trend where with the addition of Ti into $SiO_2$ the band gap drops rapidly and then only decreases slightly over the rest of the composition range. This can be expected, since the shape of the density of states (DOS) of the conduction band, which consists mostly of Ti

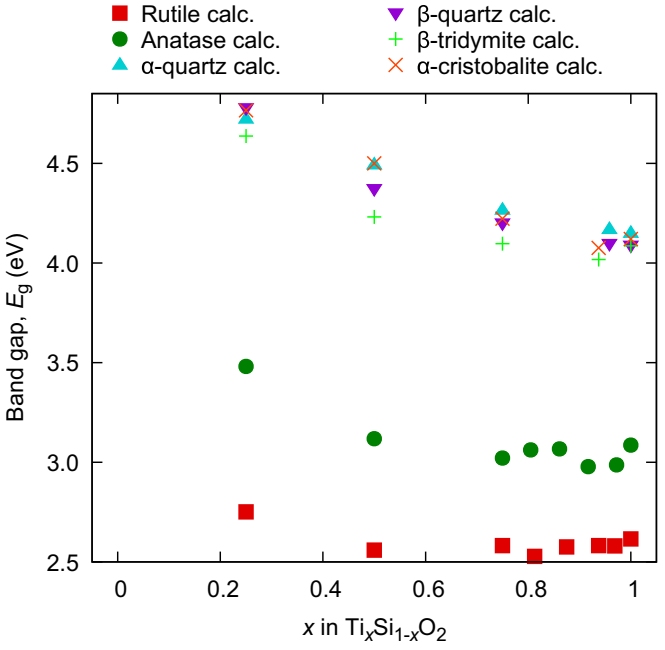


FIG. 4. Calculated electronic band gap as a function of Si content for crystalline $Ti_xSi_{1-x}O_2$ solid solutions.

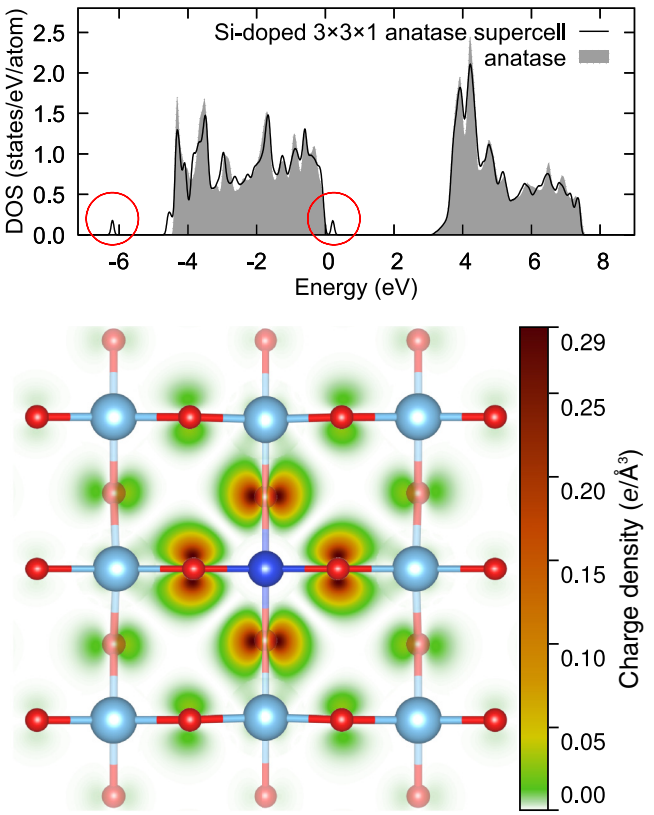


FIG. 5. Upper panel: DOS of $TiO_2$ anatase and $Ti_xSi_{1-x}O_2$ $3 \times 3 \times 1$ anatase supercell with one Si atom with highlighted separate defect states above and below the valence band. Bottom panel: Charge density of the defect state above the band gap shown in the $3 \times 3 \times 1$ supercell along the $a$ and $b$ anatase axis. Atom colors are Si: dark blue, Ti: light blue, O: red. Note that the oxygen atoms are slightly above and below the plane.

$3p$-like states and is responsible for the band gap, stays mostly at the same energy up to high Si concentrations and the band only reduces in magnitude. We can therefore conclude that the Ti-like conduction bands do not depend highly on the Ti environment (i.e., on the coordination number) and the small increase of the band gap with increasing Si concentration in the $TiO_2$-rich region is mostly due to decrease of the overall Ti $3p$-like valence bandwidth.

We note that one of the typical features of the TB-mBJ is the reduction of conduction and valence bandwidths with respect to the PBE functional [22]. In the case of $TiO_2$ it is mostly visible in opening of a second gap between the Ti $3p$-like valence states and the higher-energy states as visible in Fig. 5. This gap is present also with LDA and GGA calculations, albeit smaller, but does not show up in GW calculations [59].

The interesting feature seen in the band-gap evolution of rutile- and anatase-based solid solutions is the decrease of the band gap for small silicon concentrations. This reduction of the band gap while doping rutile or anatase with Si was already reported by Long *et al.* [60] who attributed the band-gap reduction to a downward shift of the bottom of the conduction band caused by the Si $3s$ states. We propose a different explanation for this reduction: Figure 5 shows calculated normalized total density of states for $3 \times 3 \times 1$ anatase

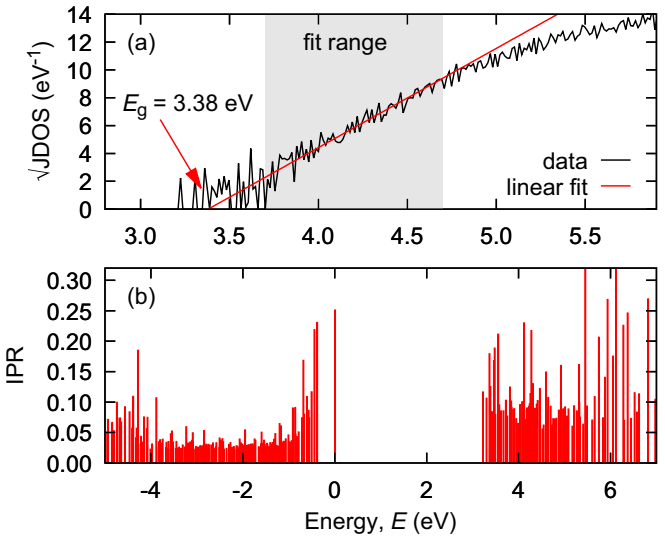


FIG. 6. Upper panel: Fit of the linear part of $\sqrt{\text{JDOS}}$ near the absorption edge for a-$Ti_{0.5}Si_{0.5}O_2$ (with fitting range highlighted). Bottom panel: Band localization at Γ point measured by inverse participation ratio for a-$Ti_{0.5}Si_{0.5}O_2$.

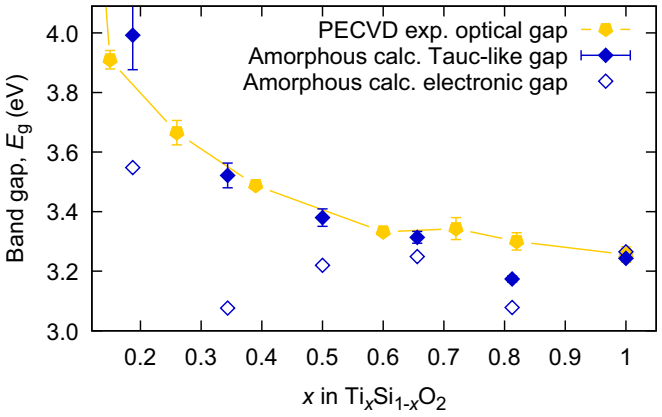


FIG. 7. Calculated Tauc-like band gap as a function of composition ratio $x$ for a-$Ti_xSi_{1-x}O_2$ together with experimental optical band gap. The line serves only to guide to the eye.

supercell with one Ti atom replaced with Si (corresponding to $x = 0.972$) as well as of pure anatase. The DOS was aligned by using the oxygen 2*s* core states energy and shows that the single silicon atom present in the supercell introduces states at the top (and at the bottom) of the valence band, separated from the rest of the valence bands, while the bottom of the conduction band remains mostly the same. The charge density of the defect state is plotted in Fig. 5, showing a high localization of this state on the oxygen atoms next to the Si site, and further highlighting that the reduction of the band gap is caused by Si-induced oxygen states rather than by the Si 3*s* states in the conduction band. The $Ti_xSi_{1-x}O_2$ rutile structure also exhibits the same behavior. Since no such decrease for band gap is visible for the hypothetical silica-based structures in the Ti-rich region, we can conclude that these defect states are a direct result of forcing the Si into an over-coordinated site.

The electronic band gap of a-$Ti_xSi_{1-x}O_2$ in Fig. 4 shows significant fluctuations. These fluctuations are caused by defect states originating from structural disorder of the amorphous structures. The defect states are highly localized as can be seen in Fig. 6 where we quantified the band localization at the Γ point by means of the inverse participation ratio (IPR) [61].

To obtain band gaps for amorphous structures comparable with optical measurements we fit the linear part of the square root of the joint density of states (JDOS) near the absorption onset. The extrapolation of this linear fit to zero JDOS determines the band-gap value with defect states filtered out. This was already used for determination of the band gap in a-$HfO_2$ [28] and an equivalent approach was also used for a-$TiO_2$ [62]. Band gaps obtained by this approach are denoted as Tauc-like gaps due to the similarity of the fitting approach to the well-known Tauc plot used experimentally to determine band gap [63]. They are shown in Fig. 7 together with values obtained directly from fitting of the optical data as one of the parameters of the dispersion model. This figure demonstrates very good agreement between the theoretically predicted and experimentally measured band-gap evolution; the values are also in line with optical band-gap values reported by others [4,5,9].

Note, however, that the Tauc-like gap calculation is still missing excitonic effects. To add them one would have to preform the calculations by using the Bethe–Salpeter equation (BSE) [64]. That was, unfortunately, computationally prohibitive due to their extreme demands combined with our rather large supercells. The inclusion of excitonic effects can be expected to decrease the optical band gap slightly, as was reported for a-$TiO_2$ where a redshift of ∼0.5 eV of the dielectric function was obtained with BSE; however, without any significant changes in the dielectric function shape [62]. Consequently, the excellent agreement between the predicted and measured band gaps is partially the result of an error cancellation; in particular, the underestimation of the TB-mBJ band gap is compensated by the RPA in optical calculations.

### D. Optical constants

All the crystalline solid solutions have up to three independent components of the dielectric tensor $\hat{\epsilon}$ due to the corresponding space group symmetry. To simplify the presentation of our results and make the calculated single-crystal properties comparable with experimental data, in the following we present an "effective" dielectric function calculated as $\varepsilon = \text{tr}(\hat{\epsilon})/3$. This models the macroscopic response of a polycrystalline material with randomly oriented grains and neglected effect of grain boundaries. For the a-$Ti_xSi_{1-x}O_2$ the three calculated diagonal component of the dielectric tensor were found to be nearly identical, hence we again show the effective dielectric function.

The calculated evolution of the imaginary part of the dielectric function $\varepsilon_i$ is shown in Fig. 8 for all seven considered polymorphs together with the experimentally measured optical response of our PECVD samples.

For the $TiO_2$-rich compositions, all the calculated spectra show two distinct peaks around 4.5 and 7.5 eV. For the octahedral based structures (i.e., anatase, rutile, and to some extent even the amorphous phase) this is a direct consequence

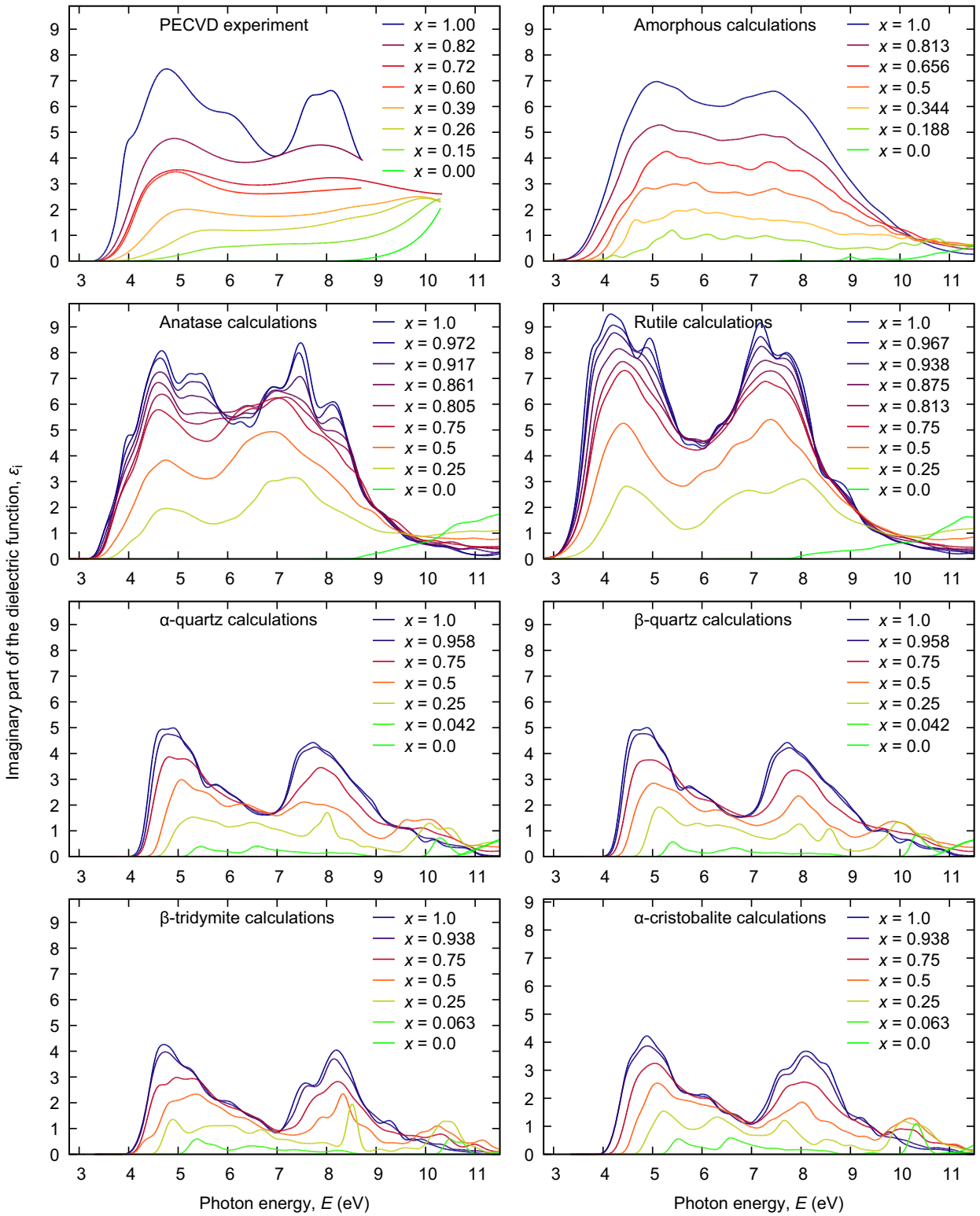


FIG. 8. Evolution of the imaginary part of the dielectric function for all calculated $Ti_xSi_{1-x}O_2$ polymorphs as well as experimental samples.

of the octahedral crystal-field splitting of the Ti 3*d* states into the $e_g$ ($d_{x^2+y^2}$, $d_{z^2}$) and $t_{2g}$ ($d_{xy}$, $d_{yz}$, $d_{xz}$) parts. The lower energy peak can be identified with interband transitions from the O 2*p*-like valence band to the $t_{2g}$-like Ti 3*d* sub-band, while the higher-energy peak originates from transitions into the $e_g$-like Ti 3*d* sub-band. For the $TiO_2$-rich crystalline solid solution based on $SiO_2$ structures two peaks are still present; however, they do not result from the tetrahedral crystal-field splitting since the analysis of the band character shows that the splitting of the *d* orbitals is negligible in this case. We propose that those two peaks are caused rather by the separation of oxygen bonding and nonbonding valence bands, leading to a

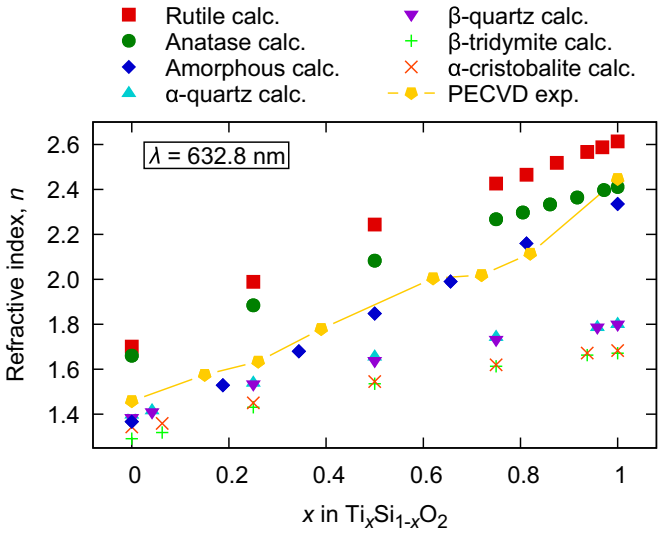


FIG. 9. Evolution of refractive index at 632.8 nm with composition for various $Ti_xSi_{1-x}O_2$ polymorphs.

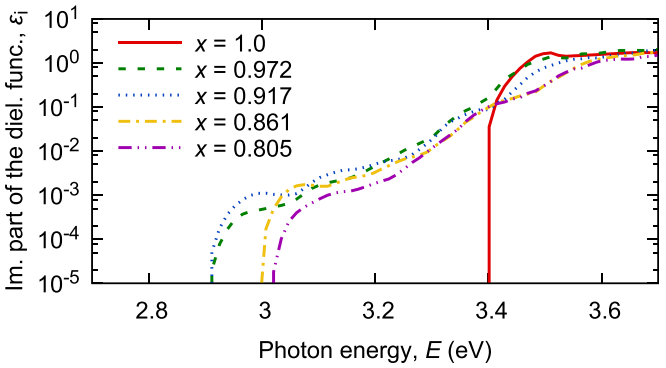


FIG. 10. Imaginary part of the calculated unbroadened dielectric function near absorption edge for anatase-based $Ti_xSi_{1-x}O_2$ solid solutions.

gap in the valence band, a feature that is typical for the $SiO_2$ polymorphs [17].

The experimental $\varepsilon_i$ again shows a two-peak structure. The first peak, around 4.8 eV for $TiO_2$, is shifting to higher energies and becoming less pronounced as the Ti/Si ratio decreases. The second peak is positioned around 8 eV; however, it is only pronounced for pure $TiO_2$ while for the rest of the compositions it is only slightly visible or not present at all. This could be attributed to the decreasing Ti content, the decrease of average Ti coordination number (and hence lower percentage of Ti in the octahedral position), and finally to the decreasing sensitivity of the optical instruments at the VUV edge of the measurement range. Comparing the shapes of the experimental dielectric functions with the calculated ones, there is a exceptional match between the calculated $\varepsilon_i$ of anatase $TiO_2$ and $\varepsilon_i$ of the $TiO_2$ film, which was determined to be an anatase polycrystal by XRD. The rest of the experimental spectra are in good agreement with the amorphous calculations especially regarding the position of the first peak and overall intensity. The only notable difference is the position of the second peak, which is shifted to slightly lower energies in the calculations. We attribute this to the above-mentioned contraction of the valence band caused by TB-mBJ.

The evolution of calculated and experimental refractive index at the He-Ne laser wavelength 632.8 nm as a function of $x$ is shown in Fig. 9. The calculated refractive index for a-$Ti_xSi_{1-x}O_2$ is a near perfect match for the experimental values, and only slightly deviates at the ends of the composition spectra. For pure $TiO_2$, the experimental value of the refractive index matches well the calculated value of anatase, making the predicted and measured optical response consistent with the structural analysis in Sec. III B. On the $SiO_2$ side the calculated refractive index is slightly underestimated with respect to the experiment. We believe that this small discrepancy is caused by more pronounced excitonic effects in $SiO_2$, e.g., the missing redshift of the spectral weight due to the neglect of excitonic effects in the RPA is larger and hence no longer fully compensated by the TB-mBJ. This leads to a shift of the spectral weight to higher energies and hence lower refractive index.

To justify the Tauc-plot approach for the band-gap estimates with the defect states filtered out, we examine the effect of the defect states in the band gap on the optical absorption near the absorption onset. Detailed analysis of the unbroadened dielectric function for the Si-doped anatase and rutile $Ti_xSi_{1-x}O_2$, where the defects are most pronounced, reveals that absorption near the absorption onset is quite weak and increases very slowly (Fig. 10). This can be due to the fact that, at the top of the valence band, there are mostly Si-induced states localized at O sites, while the bottom of the conduction band is populated mostly with Ti states. Hence, the resulting momentum matrix elements are small. This on one hand explains an apparent discrepancy between the raw calculated and measured results, and on the other hand supports the application of the Tauc-plot method. The extremely weak absorption near the edge onset is below the sensitivity of our ellipsometric and spectrophotometric measurements.

## IV. CONCLUSIONS

Using density functional theory with the PBE functional, we constructed structural models of amorphous and crystalline $Ti_xSi_{1-x}O_2$ solid solutions over the whole compositional range. The models were used with the recently developed TB-mBJ potential to calculate compositionally dependent optical properties at the RPA level. Our predictions were confronted with experimental optical measurements of PECVD-deposited $Ti_xSi_{1-x}O_2$ films from the near infrared up to the VUV region yielding a satisfactory agreement. In particular, the predicted band-gap dependence on the composition matches well the measured trend including absolute band-gap values. Defect states in the band gap were observed and explained as oxygen states, localized near Si sites. We also showed that the influence of those states on the overall absorption is negligible. Furthermore, we explained the nonlinear behavior of the band-gap evolution due to the Ti $3d$ states being mostly unaffected by the changes in the average Ti environment up to high Si concentrations. A good agreement between calculated and experimental imaginary part of dielectric function was observed for the amorphous structures. We were able to describe the two-peak structure observed in $\varepsilon_i$ as a result of

the octahedral crystal-field splitting of the Ti 3*d* states for the octahedral-based compounds and as a result of splitting of the valence O states in the tetrahedral based structures. All of this shows that using the relatively simple TB-mBJ + RPA approach for the calculation of the optical properties of $Ti_xSi_{1-x}O_2$ gives, despite some shortcomings, highly relevant results and can successfully explain the majority of features seen in the experimental measurements.

## ACKNOWLEDGMENTS

This work has been supported by the Ministry of Education, Youth and Sports of the Czech Republic under the project CEITEC 2020 (LQ1601), by the MOBILITY projects 7AMB15AT017 and 7AMB15FR036 funded by Czech Ministry of Education, Youth and Sports (CMEYS), by the project CZ09/2015 funded by the Austrian Agency for International Cooperation in Education and Research (OeAD-GmbH), and by the Ministry of Education, Youth and Sports from the Large Infrastructures for Research, Experimental Development and Innovations project "IT4Innovations National Supercomputing Center - LM2015070". The computational results presented have been achieved [in part] by using the Vienna Scientific Cluster (VSC). Part of the work was carried out with the support of CEITEC Nano Research Infrastructure (MEYS CR, 2016-2019). This work has also been supported by the French MAEDI and MENESR ministries under the project PHC Barrande No. 34006WK.

[1] J. A. Dobrowolski, D. Poitras, P. Ma, H. Vakil, and M. Acree, Appl. Opt. **41**, 3075 (2002).
[2] S. Chao, W.-H. Wang, and C.-C. Lee, Appl. Opt. **40**, 2177 (2001).
[3] D. Poitras, S. Larouche, and L. Martinu, Appl. Opt. **41**, 5249 (2002).
[4] F. Gracia, F. Yubero, J. Holgado, J. Espinos, A. Gonzalez-Elipe, and T. Girardeau, Thin Solid Films **500**, 19 (2006).
[5] H. Demiryont, Appl. Opt. **24**, 2647 (1985).
[6] J.-S. Chen, S. Chao, J.-S. Kao, H. Niu, and C.-H. Chen, Appl. Opt. **35**, 90 (1996).
[7] T. DiStefano and D. Eastman, Solid State Commun. **9**, 2259 (1971).
[8] H. Tang, H. Berger, P. E. Schmid, and F. Lévy, Solid State Commun. **92**, 267 (1994).
[9] D. Li, S. Elisabeth, A. Granier, M. Carette, A. Goullet, and J.-P. Landesman, Plasma Processes Polym. **13**, 918 (2016).
[10] M. Bahtat, J. Mugnier, C. Bovier, H. Roux, and J. Serughetti, J. Non-Cryst. Solids **147–148**, 123 (1992).
[11] X. Wang, H. Masumoto, Y. Someno, and T. Hirai, Thin Solid Films **338**, 105 (1999).
[12] J. Muscat, V. Swamy, and N. M. Harrison, Phys. Rev. B **65**, 224112 (2002).
[13] M. Iuga, G. Steinle-Neumann, and J. Meinhardt, Eur. Phys. J. B **58**, 127 (2007).
[14] M. A. Caravaca, J. C. Miño, V. J. Pérez, R. A. Casali, and C. A. Ponce, J. Phys.: Condens. Matter **21**, 015501 (2009).
[15] S.-D. Mo and W. Y. Ching, Phys. Rev. B **51**, 13023 (1995).
[16] G. Sai and L. Bang-Gui, Chin. Phys. B **21**, 057104 (2012).
[17] S. S. Nekrashevich and V. A. Gritsenko, Phys. Solid State **56**, 207 (2014).
[18] E. K. Chang, M. Rohlfing, and S. G. Louie, Phys. Rev. Lett. **85**, 2613 (2000).
[19] M. Landmann, T. Köhler, E. Rauls, T. Frauenheim, and W. G. Schmidt, J. Phys.: Condens. Matter **26**, 253201 (2014).
[20] A. B. Rosenthal and S. H. Garofalini, J. Non-Cryst. Solids **107**, 65 (1988).
[21] F. Tran and P. Blaha, Phys. Rev. Lett. **102**, 226401 (2009).
[22] D. J. Singh, Phys. Rev. B **82**, 205102 (2010).
[23] D. Koller, F. Tran, and P. Blaha, Phys. Rev. B **85**, 155109 (2012).
[24] K. Momma and F. Izumi, J. Appl. Crystallogr. **44**, 1272 (2011).
[25] A. Zunger, S.-H. Wei, L. G. Ferreira, and J. E. Bernard, Phys. Rev. Lett. **65**, 353 (1990).
[26] T. Zhu and S.-P. Gao, J. Phys. Chem. C **118**, 11385 (2014).
[27] D. A. Drabold, Eur. Phys. J. B **68**, 1 (2009).
[28] P. Ondračka, D. Holec, D. Nečas, and L. Zajíčková, J. Phys. D: Appl. Phys. **49**, 395301 (2016).
[29] O. Anderson, C. R. Ottermann, R. Kuschnereit, P. Hess, and K. Bange, Fresenius' J. Anal. Chem. **358**, 315 (1997).
[30] B. Prasai, B. Cai, M. K. Underwood, J. P. Lewis, and D. A. Drabold, J. Mater. Sci. **47**, 7515 (2012).
[31] G. Kresse and J. Furthmüller, Phys. Rev. B **54**, 11169 (1996).
[32] G. Kresse and J. Furthmüller, Comput. Mater. Sci. **6**, 15 (1996).
[33] G. Kresse and D. Joubert, Phys. Rev. B **59**, 1758 (1999).
[34] J. P. Perdew, K. Burke, and M. Ernzerhof, Phys. Rev. Lett. **77**, 3865 (1996).
[35] H. J. Monkhorst and J. D. Pack, Phys. Rev. B **13**, 5188 (1976).
[36] P. Blaha, K. Schwarz, G. Madsen, D. Kvasnicka, and J. Luitz, WIEN2k, An Augmented Plane Wave + Local Orbitals Program for Calculating Crystal Properties (Karlheinz Schwarz, Techn. Universität Wien, Austria, 2001), ISBN 3-9501031-1-2.
[37] C. Ambrosch-Draxl and J. O. Sofo, Comput. Phys. Commun. **175**, 1 (2006).
[38] A. Granier, F. Nicolazo, C. Vallée, A. Goullet, G. Turban, and B. Grolleau, Plasma Sources Sci. Technol. **6**, 147 (1997).
[39] S. O. Rice, Commun. Pure Appl. Math. **4**, 351 (1951).
[40] D. Franta and I. Ohlídal, Opt. Commun. **248**, 459 (2005).
[41] D. Franta, D. Nečas, and I. Ohlídal, Appl. Opt. **54**, 9108 (2015).
[42] D. Franta, D. Nečas, and L. Zajíčková, Thin Solid Films **534**, 432 (2013).
[43] D. Franta, D. Nečas, L. Zajíčková, I. Ohlídal, J. Stuchlík, and D. Chvostová, Thin Solid Films **539**, 233 (2013).
[44] D. Franta, A. Dubroka, C. Wang, A. Giglia, J. Vohánka, P. Franta, and I. Ohlídal, Appl. Surf. Sci. (2017), doi:10.1016/j.apsusc.2017.02.021.
[45] E. Palik, *Handbook of Optical Constants of Solids* (Academic Press, Orlando, 1985).
[46] D. Franta *et al.*, Software for Optical Characterization newAD2 (2014), http://newad.physics.muni.cz.
[47] "O-Ti binary phase diagram 0–100 at.% Ti: Datasheet from "Pauling file multinaries edition—2012" in Springer Materials (http://materials.springer.com/isp/phase-diagram/docs/c_1600380), Copyright 2016 Springer-Verlag Berlin Heidelberg &

Material Phases Data System (MPDS), Switzerland & National Institute for Materials Science (NIMS), Japan.
[48] M. E. Arroyo-de Dompablo, A. Morales-García, and M. Taravillo, J. Chem. Phys. **135**, 054503 (2011).
[49] N. H. Vu, H. V. Le, T. M. Cao, V. V. Pham, H. M. Le, and D. Nguyen-Manh, J. Phys.: Condens. Matter **24**, 405501 (2012).
[50] T. Demuth, Y. Jeanvoine, J. Hafner, and J. G. Ángyán, J. Phys.: Condens. Matter **11**, 3833 (1999).
[51] A. R. Oganov and C. W. Glass, J. Chem. Phys. **124**, 244704 (2006).
[52] J. Pascual, J. Camassel, and H. Mathieu, Phys. Rev. B **18**, 5606 (1978).
[53] H. Tang, H. Berger, P. Schmid, F. Lévy, and G. Burri, Solid State Commun. **87**, 847 (1993).
[54] H. Tang, F. Lévy, H. Berger, and P. E. Schmid, Phys. Rev. B **52**, 7771 (1995).
[55] R. Asahi, Y. Taga, W. Mannstadt, and A. J. Freeman, Phys. Rev. B **61**, 7459 (2000).
[56] K. M. Glassford and J. R. Chelikowsky, Phys. Rev. B **46**, 1284 (1992).
[57] Y. Tezuka, S. Shin, T. Ishii, T. Ejima, S. Suzuki, and S. Sato, J. Phys. Soc. Jpn. **63**, 347 (1994).
[58] S. Rangan, S. Katalinic, R. Thorpe, R. A. Bartynski, J. Rochford, and E. Galoppini, J. Phys. Chem. C **114**, 1139 (2010).
[59] M. Landmann, E. Rauls, and W. G. Schmidt, J. Phys.: Condens. Matter **24**, 195503 (2012).
[60] R. Long, Y. Dai, G. Meng, and B. Huang, Phys. Chem. Chem. Phys. **11**, 8165 (2009).
[61] R. Atta-Fynn, P. Biswas, P. Ordejón, and D. A. Drabold, Phys. Rev. B **69**, 085207 (2004).
[62] M. Landmann, T. Köhler, S. Köppen, E. Rauls, T. Frauenheim, and W. G. Schmidt, Phys. Rev. B **86**, 064201 (2012).
[63] O. Stenzel, *The Physics of Thin Film Optical Spectra: An Introduction* (Springer, Berlin, New York, 2005).
[64] E. E. Salpeter and H. A. Bethe, Phys. Rev. **84**, 1232 (1951).